Journal of Geophysical Research: Planets

RESEARCH ARTICLE
10.1029/2018JE005709

# The O($^1$S) 297.2-nm Dayglow Emission: A Tracer of $CO_2$ Density Variations in the Martian Lower Thermosphere

**L. Gkouvelis[1], J.-C. Gérard[1], B. Ritter[1,2], B. Hubert[1], N. M. Schneider[3], and S. K. Jain[3]**

[1]LPAP, STAR Institute, Université de Liège, Liege, Belgium, [2]Royal Observatory of Belgium, Brussels, Belgium, [3]LASP, University of Colorado Boulder, Boulder, CO, USA

**Key Points:**
- Limb observations of the O($^1$S-$^3$P) dayglow by MAVEN confirm existence of previously predicted emission peak near 80 km
- We successfully model the lower peak emission profile and show that it only depends on the vertical $CO_2$ distribution and solar Ly-alpha
- Combination of model and observations enable to constrain the slant $CO_2$ column over the peak and the corresponding atmospheric pressure

**Correspondence to:**
L. Gkouvelis,
l.gkouvelis@uliege.be

**Citation:**
Gkouvelis, L., Gérard, J.-C., Ritter, B., Hubert, B., Schneider, N. M., & Jain, S. K. (2018). The O($^1$S) 297.2-nm dayglow emission: A tracer of $CO_2$ density variations in the Martian lower thermosphere. *Journal of Geophysical Research: Planets*, *123*. https://doi.org/10.1029/2018JE005709

Received 1 JUN 2018
Accepted 13 NOV 2018
Accepted article online 21 NOV 2018



**Abstract** The O($^1$S) metastable atoms can radiatively relax by emitting airglow at 557.7 and 297.2 nm. The latter one has been observed with the Imaging Ultraviolet Spectrograph onboard the Mars Atmosphere and Volatile Evolution Mars orbiter since 2014. Limb profiles of the 297.2-nm dayglow have been collected near periapsis with a spatial resolution of 5 km or less. They show a double-peak structure that was previously predicted but never observed during earlier Mars missions. The production of both 297.2-nm layers is dominated by photodissociation of $CO_2$. Their altitude and brightness is variable with season and latitude, reflecting changes in the total column of $CO_2$ present in the lower thermosphere. Since the lower emission peak near 85 km is solely produced by photodissociation, its peak is an indicator of the unit optical depth pressure level and the overlying $CO_2$ column density. Its intensity is directly controlled by the Lyman-α solar flux reaching the Martian upper atmosphere. We take advantage of the Lyman-α flux measurements of the solar Extreme Ultraviolet Monitor instrument onboard Mars Atmosphere and Volatile Evolution to model the observed OI 297.2-nm limb profiles. For this, we combine photodissociation sources with chemical processes and photoelectron impact excitation. To determine the relative importance of the excitation processes, we apply the model to the atmospheric structure measured by the Viking 1 lander before applying it to a model atmosphere. We find very good agreement with the lower peak structure and intensity if the $CO_2$ density provided by the Mars Climate Database is scaled down by a factor between 0.50 and 0.66. We also determine that the previously uncertain quantum yield for production of O($^1$S) atoms by photodissociation of $CO_2$ at Lyman-α wavelength is about 8%.

**Plain Language Summary** We analyze the altitude distribution of the oxygen emission at 297.2 nm observed in the Martian dayside atmosphere with the Imaging Ultraviolet Spectrograph onboard the Mars Atmosphere and Volatile Evolution orbiter. This emission is mostly produced by the interaction of solar ultraviolet radiation with the $CO_2$-dominated atmosphere above 60 km. We show that this emission has two intensity peaks. The altitude of the lower one is entirely controlled by the amount of carbon dioxide crossed by the bright solar Lyman-alpha line. We determine what fraction of $CO_2$ dissociation leads to the 297.2-nm emission and derive a relationship between the altitude of the maximum brightness and its pressure level. Comparisons with the predictions of the Mars Climate Model indicate that this model overestimates the amount of carbon dioxide in the 65–85-km region by a factor of about 2. Global monitoring and accurate modeling of the atmospheric pressure in this region of the atmosphere and its seasonal and latitudinal variations are important to understand the large-scale dynamics and for future space missions. Our results provide a method to constrain the Martian atmospheric structure in a region that is largely unexplored by other experimental methods.

## 1. Introduction

The oxygen line at 297.229 nm is one of the two emissions from the metastable O($^1$S) state. It corresponds to the OI $^3$P-$^1$S singlet magnetic dipole transition with a transition probability of $7.54 \times 10^{-2}$ s$^{-1}$ (NIST database; Kramida et al., 2018). The other transition leads to the $^1$D metastable state and is associated with the auroral "green line" doublet at 557.7 nm. The combined radiative lifetime of O($^1$S) atoms is 0.8 s (Froese-Fischer & Tachiev, 2004). The 297.2-nm line is relatively easy to observe at the planetary limb at medium spectral resolution following proper subtraction of the solar scattered sunlight. It was first observed in the Martian atmosphere with the ultraviolet spectrometer during the Mariner 6 and 7 flybys (Barth et al., 1971; Stewart, 1972) and later from the Mariner 9 orbiter (Barth et al., 1972; Stewart et al., 1972). The spectral resolution was about 2 nm. The limb profiles showed a single peak near 120 km reaching peak intensities of ~2 kR.

Further observation with the Investigation of the Characteristics of the Atmosphere of Mars (SPICAM) spectrograph onboard Mars Express at 1.5-nm resolution allowed detection of this emission above 120 km (Leblanc et al., 2006) with a limited signal-to-noise ratio. The intensity was weaker in the SPICAM data relative to other emissions in comparison with the Mariner 9 data. Leblanc et al. (2006) detected the presence of the OI 297.2-nm emission in dayglow spectra obtained with SPICAM, but the brightness relative to the $CO_2$ UV doublet at 289 nm was less than in the Mariner spectra.

The production of the O($^1$S) atoms in the Martian dayglow was first modeled by Fox and Dalgarno (1979) for the low solar activity conditions prevailing during the Viking 1 landing and a solar zenith angle of 45° (Hanson et al., 1977; Nier & McElroy, 1977). They predicted that the bulk of the O($^1$S) production was from dissociative excitation of $CO_2$ by extreme ultraviolet (EUV) solar radiation followed by dissociative recombination of $CO_2^+$ ions, electron impact on $CO_2$, and electron impact on O atoms. They calculated a total vertical brightness of 638 Rayleighs. They predicted the presence of a peak near 137 km, but they also foresaw the existence of a second brighter maximum near 90 km resulting from the dissociation of $CO_2$ by solar Lyman-α radiation. They explained the presence of the lower peak by the deeper penetration of this radiation into the Martian lower thermosphere. This is a consequence of the low value of the $CO_2$ absorption cross section at 121.6 nm, coupled with the high intensity of the solar Lyman-α emission. Further modeling of the Martian 297.2-nm dayglow emission by Simon et al. (2009) and Gronoff et al. (2012) also produced a double-peak structure in the emission profile but, contrary to Fox and Dalgarno, they calculated an upper peak brighter than the low-altitude maximum. In contrast, Huestis et al. (2010) argued that the different scale heights of the OI 297.2-nm and the $CO_2^+$ airglow emissions indicates that photodissociation of $CO_2$ is not the dominant source of O($^1$S) atoms relative to $O_2^+$ dissociative recombination. This conclusion was challenged by Gronoff et al. (2012) and Jain (2013), who showed that the scale heights of the different emissions were compatible. In contrast, they concluded that an unrealistic $O_2^+$ density would be required for $O_2^+$ recombination to play a significant role in the production of the 297.2-nm emission.

The Imaging Ultraviolet Spectrograph (IUVS) instrument (McClintock et al., 2015) onboard the Mars Atmosphere and Volatile Evolution (MAVEN) Mars orbiter provided the first limb profiles of the OI 297.2-nm emission down to 75 km (Jain et al., 2015). They found clear indication that the predicted lower peak exists, but it was too early in the MAVEN mission to present definite results. The IUVS instrument has collected ultraviolet airglow spectra near periapsis since October 2014. In this study, we present a few examples of 297.2-nm dayglow observed limb profiles at different Martian seasons. We describe the main features of the airglow model used to calculate the O($^1$S) production rate for the conditions of the IUVS observations. We examine the sources of O($^1$S) atoms as a function of altitude and show that $CO_2$ photodissociative excitation is the dominant source of O($^1$S) atoms in the range 70–200 km and the only significant source of the lower emission peak. The intensity limb profiles calculated using the Lyman-α solar irradiance directly measured by the EUV monitor onboard MAVEN are then compared with the IUVS observations. The $CO_2$ column density is scaled to best fit the altitude of the lower peak. We show that observations of the altitude of the OI 297.2-nm dayglow are sensitive indicators of the overlying column density of $CO_2$ and may be used as a tool to monitor seasonal and latitudinal changes of the $CO_2$ density and changes of the altitude of the pressure levels.

## 2. Observations

The IUVS is one of the eight scientific instruments onboard the MAVEN satellite. It supports two spectroscopic modes, using two separate gratings that provide the required resolving powers. One of the two operates near normal incidence and covers the 110–340-nm range with a resolving power ~250. The second one uses a prism cross-disperser and an echelle grating to cover the 120–131-nm range. IUVS is operated in five different observation modes: stellar occultation, atmospheric limb scans, echelle, disk mapping, and Martian corona observations. In this work, we are interested in limb scan observations, and we use only the normal incidence spectroscopy which is divided in two channels, FUV and MUV. The ultraviolet light is dispersed by the grating into the above two diffraction orders. Finally, the light passes through the entrance slit with a 0.06° × 11° field of view and reaches the detector. The emission of interest here is detected in the MUV channel with a spectral resolution of 1.2 nm and dispersion of 7.27 nm/mm. The noise sources are photon-counting noise, detector dark current noise, quantization noise, intensifier excess noise, and detector read noise (McClintock et al., 2015). The calibration of the spectra is based on ground tests as well as in-flight measurements using UV

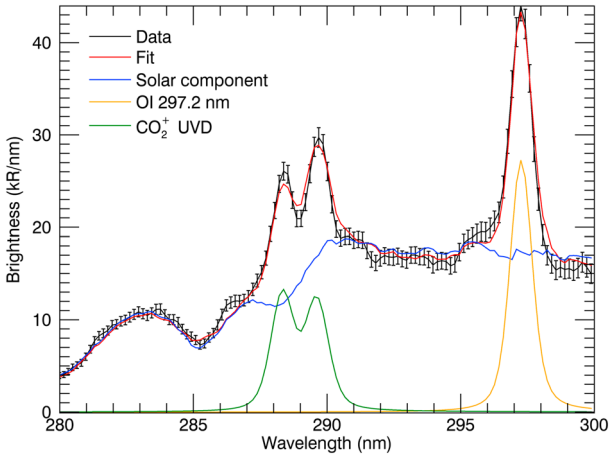


**Figure 1.** An example of IUVS-MUV spectrum in the 280–300-nm range at 77 km. The solar background contribution in shown in blue and the extracted contribution of the $CO_2^+$ UVD doublet and the OI 297.2-nm emissions in green and yellow, respectively.

bright stellar targets with well-known spectral fluxes. For the MUV channel, the systematic uncertainties are estimated to be on the order of 25% (Jain et al., 2015; Schneider et al., 2015; Stevens et al., 2015). More details of the instrument properties and the observation modes may be found in McClintock et al. (2015). During periapsis observations, the altitude of the spacecraft is less than 500 km. The observations were performed with the detector looking in a direction almost parallel to the surface and the slit oriented horizontally. IUVS is equipped with a rotating mirror that allows 21 different positions so that it can perform limb observations at different altitudes as it passes close to or inside the atmosphere. Therefore, each scan provides a limb profile of the different spectral features. During each orbit IUVS performs a maximum of 12 scans. Figure 1 shows a part of an MUV spectra collected in limb mode observed at 77-km altitude during orbit 3000. The 297.2-nm emission is clearly apparent next to the $CO_2^+$ UV doublet.

The data used in this study have been downloaded from NASA's Planetary Data System archives. Three different processing levels of the data are available. Level 1A data corresponds to the raw instrument readouts in data numbers per bin. Level 1B data provide calibrated instrument readouts in kR/nm and include background subtraction and ancillary data. Level 1C data include calibrated brightness of individual emissions that has been reduced by isolating emission features and spatial binning to facilitate processing: the dayglow spectra include many different atomic and molecular emissions, including the spectral feature from oxygen at 297.2 nm. Each emission may be identified by its wavelength and its expected relative intensity. The brightness of any atomic or molecular feature is determined by using a multiple linear regression method to fit the various components of each observed spectrum following convolution with the instrumental line spread function (Stevens et al., 2015). In addition to these atomic and molecular emissions, the fit templates also include a reflected solar spectrum. This solar scattered light component becomes important for limb observations with tangent point altitudes below about 100 km, especially in the longer-wavelength segment of the MUV spectra. In this region, reflection by high-altitude clouds and dust as well as stray light within the instrument can contribute to the background signal (Stevens et al., 2015; Schneider et al., 2015; Jain et al., 2015). The IUVS team uses a high signal-to-noise ratio average solar spectrum, measured by the IUVS instrument, in the multiple linear regression analysis to calculate the brightness of various emissions provided in the level 1c data. The shape of this solar scattered light component is an excellent estimate of the scattered light embedded in the airglow signal and efficiently removes the solar stray light at these altitudes. In addition, the 297.2-nm emission and nearby $CO_2^+$ UV doublet bands have sufficient brightness (Figure 1) to guarantee a high signal-to-noise ratio in the region of the lower emission peak. For a bright case (36 kR), the signal-to-noise ratio is 17 at 67.5 km, 72 at 87.5 km, and 70 at 120 km. For a weak case (26 kR), the signal-to-noise ratio is 12 at 67.5 km, 72 at 87.5 km, and 48 at 120 km. These values refer to a single scan.

The step from level 1B to 1C involves also combining separate exposures into single-altitude profiles. In order to do this, regular 5-km altitude bins are defined. The wavelength scale and dispersion relation are derived by fitting the composite blended spectrum to limb spectra near the airglow peak. The spectral shape of the features is based on IUVS observations of Lyman-$\alpha$ immediately after orbital insertion. Hence, the level 1C data provide the limb intensities of major FUV and MUV emissions as a function of the tangent point altitude of the IUVS line of sight. They are given in one file per orbit and they contain for each spectral feature 65 altitude bins per scan, grouped into 5-km bins. The altitude range varies in each scan depending on the position of the spacecraft on its orbit at the time of the observation. For this study, we used IUVS archive release versions V07 up to orbit 5679 and V12 for orbits 5680 to 6073 corrected by a factor of 0.69 at 297.2 nm following the calibration revision made in November 2018.

MAVEN has been operating since November 2014 and at the time of writing has collected more than 1.5 Martian years of observations. In this study, we used level 1C processed data from November 2014 up to January 2018. This data set includes observations from about 6000 orbits, covering all ranges of latitudes, solar zenith angles, and almost all solar longitudes. Thus, for this study, samples corresponding to various

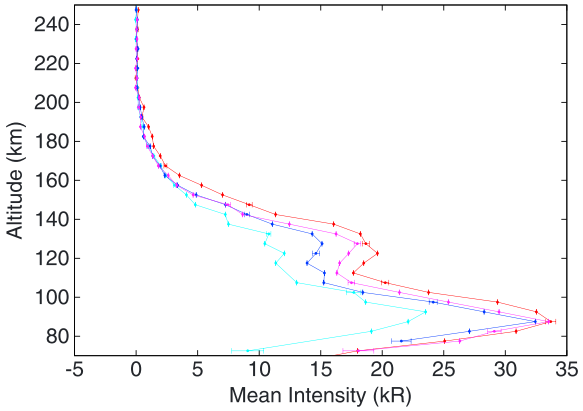


**Figure 2.** Example of limb OI 297.2-nm limb profiles observed during orbit 1051, on 25 April 2015. The solar zenith angle varied from 40° (purple) to 10° (orange) during these measurements. The horizontal bars indicate the 1-σ statistical experimental uncertainty.

conditions could be selected in order to create average limb profiles that we use to characterize the emission and its variations for comparison with model simulations.

## 3. Examples of Limb Profiles

Figure 2 shows individual limb scans of the OI 297.2-nm line emission collected along a single orbit. The data illustrate the evolution of the limb profiles with changing solar zenith angle between individual scans between 10° and 40°. Table 2 presents details on the observational conditions of the four samples that are selected for this study. The four average vertical profiles that were created by selecting individual vertical scans meeting these conditions are plotted in Figure 3 with red dots and 1-σ variability bars associated with each data point.

Our selected samples cover a wide range of the so far overall MAVEN mission seasons and latitudes. We detect a variability of ~30% in the intensity within a SZA subgroup and about 20 km in the altitude of the peak. We can clearly detect a double peak in the observations, as was suggested by Jain et al. (2015), at solar zenith angles less than 60°. For the data we have studied, the upper peak appears in the altitude range of 108–128 km and the lower main peak at 75–95 km. We find an intensity ratio of the lower to the upper peak between 2 and 2.5, but we cannot confirm a constant value at this point. Even though the limb profiles are provided with a fixed altitude resolution of 5 km, it is possible to better determine the altitude of the peak by fitting a curve to the level 1c data (Figure 4) and achieve higher-altitude sensitivity in the variability study. For this purpose, we choose a quadratic function, which is the first-order development of a Chapman layer near its maximum

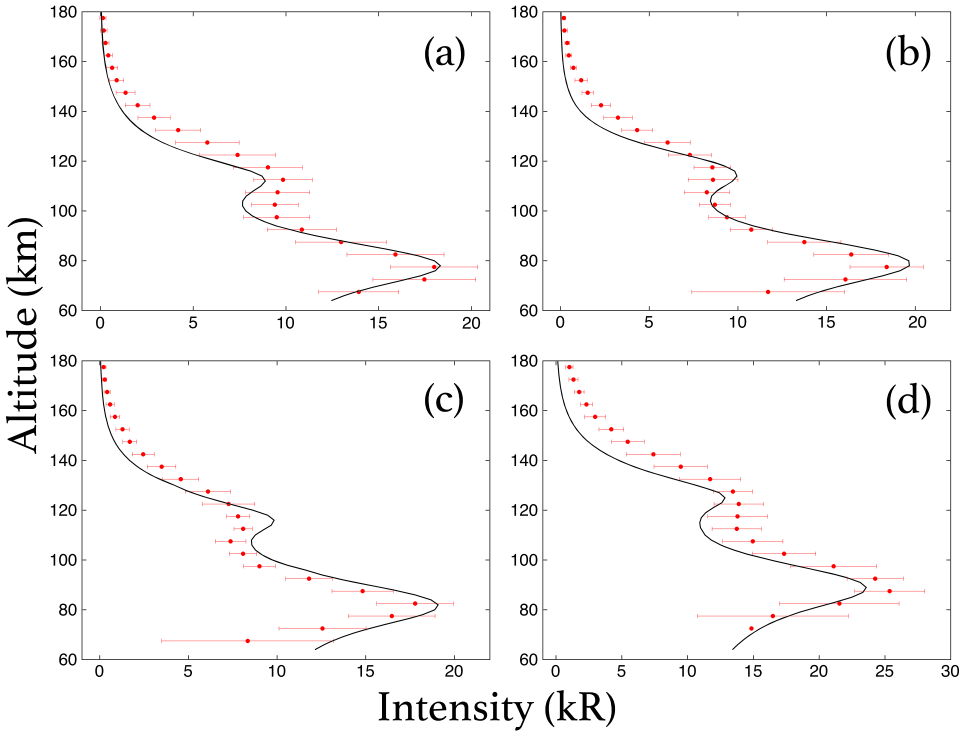


**Figure 3.** OI 297.2-nm airglow limb intensity measured from IUVS/MAVEN in different conditions (red dots). The red horizontal bars indicate the 1-σ variability of the mean limb intensity at each selected altitude level. The model simulations are shown as a black solid line. The corresponding solar longitude, latitude, average solar zenith angle, and period for each average profile are listed in Table 2, together with the observed lower peak altitude and $CO_2$ column scaling factors relative to the values of the Mars climate database (MCD).

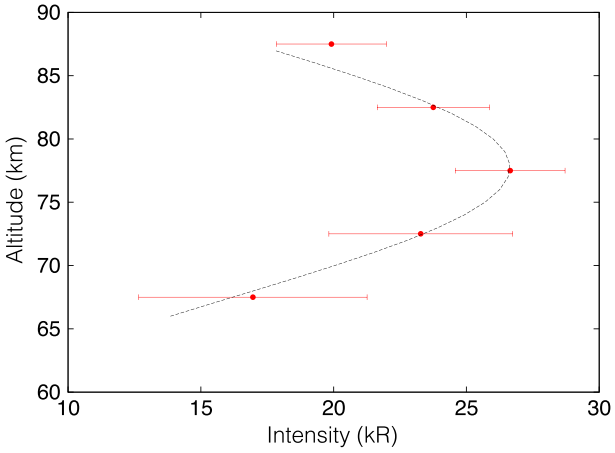


**Figure 4.** Example of an average of 57 limb profiles used to build case (b) in Figure 3 (red dots) and fitted second order curve near the emission peak (black dotted line). The horizontal bars indicate the 1-σ signal variability at each altitude.

(Chamberlain & Hunten, 1990). The Chapman formalism is appropriate here as a monochromatic radiation (Ly-α) produces the layer and $CO_2$ is both the source of metastable atoms and the sole Ly-α absorber. Further justification for this approach is given in details in section 4.2 where we discuss the modeling of the vertical profile.

## 4. Modeling of the OI 297.2-nm Emission

First, we describe the sources and sinks of metastable O($^1$S) atoms. We then provide a short description of the numerical model used to calculate the 297.2-nm volume emission rate and simulate limb observations from the IUVS instrument. Finally, we compare examples of calculated limb profiles with the IUVS observations described in section 3.

### 4.1. Sources and Sinks of O($^1$S) Atoms

We use a detailed airglow model of the sources and sinks of the O($^1$S) atoms to understand the significance of the observed changes in the 297.2-nm airglow brightness and to use it as a diagnostic of the global distribution of $CO_2$ and its changes. Following Fox and Dalgarno (1979), the main sources of O($^1$S) atoms in the Martian upper atmosphere are listed in Table 1.

In this table, $e_{th}$ designates thermal electrons; $e_{pe}$ the photoelectrons; $QY_1$, $QY_2$, and $QY_3$ the quantum efficiencies of processes (1), (2), and (6) for the production of O($^1$S) atoms; and $\sigma_1$, $\sigma_2$, and $\sigma_3$ the excitation cross sections for electron collisions with ground state $CO_2$, O, and CO, respectively.

Radiative relaxation occurs through emission of the OI 557.7-nm doublet and the 297.2-nm line. The branching ratio between the two transitions has been modeled from quantum mechanics ab initio principles (NIST; Kramida et al., 2018). Results are reasonably consistent with each other and in fair agreement with laboratory measurements. A value of the $R = A_{555.7\ nm}/A_{297.2\ nm}$ ratio equal to 16.7 was recommended by NIST, based on the ab initio calculations. Observations of both emissions in airglow and aurora have led to lower values, with a nightglow determination of $R = 9.8 \pm 1.0$ by Slanger et al. (2006) and an auroral value of $R = 9.3 \pm 0.5$ by Gattinger et al. (2009). A recent calculation by Chantler et al. (2013) uses the multiconfiguration Dirac–Hartree–Fock method. Their calculations were made in both the length and velocity gauges so that their accuracy could be monitored by the gauge convergence. Despite differences between their method and those of previous authors, their results consistently provide a $R$ ratio close to 15.5 within a few percent. We use this value in our model as it is in close agreement with several earlier ab initio calculations and the NIST recommendation.

The total transition probability from the $^1$S state is 1.34 s. Below ~100 km, collisional deactivation of O($^1$S) atoms becomes important. We adopt quenching coefficients $k_{CO2} = 3.2 \times 10^{-11}\ \exp(-1{,}323/T)$ cm$^3$/s for $CO_2$, $k_{CO} = 7.4 \times 10^{-14}\ \exp(-957/T)$ cm$^3$/s for CO from Capetanakis et al. (1993), and $k_O < 1.2 \times 10^{-14}$ cm$^3$/s (Krauss & Neumann, 1975; Slanger & Black, 1981) for O($^3$P) atoms. Based on these values, quenching by $CO_2$ is dominant relative to other collisional deactivation processes in the lower thermosphere. However, its efficiency remains less than 10% of the total radiative transition probability $A_{tot}$ (1.34 s) above ~70 km. The volume emission rate of 297.2-nm photons at each altitude is then given by

$$\eta(297.2\ \text{nm}) = P\left[O(^1S)\right]\left(A_{297.2}/A_{tot}\right)\left(A_{tot}/\left(A_{tot} + k_{CO2}\left[CO_2\right] + k_O\left[O\right] + k_{CO}\left[CO\right]\right)\right) \quad (7)$$

where P [O($^1$S)] is the total volume production rate of O($^1$S) atoms and $A_{tot}$ is the sum $A_{297.2\ nm} + A_{557.7\ nm}$ of the transition probabilities of the O($^1$S) → O($^3$P) and O($^1$S) → O($^1$D) transitions, respectively.

**Table 1**
*Sources of O($^1$S) Atoms and Key Quantities*

| Process | Quantity | Quantum Yield | Number |
|---|---|---|---|
| $CO_2$ + photons → CO + O($^1$S) | EUV flux<br>Ly-α flux | $QY_1$ (see Figure 5)<br>$QY_{Ly\text{-}\alpha} = 0.075$ | (1) |
| $e_{pe} + CO_2$ → CO + O($^1$S) | $\sigma_1$ | | (2) |
| $e_{pe}$ + O($^3$P) → O($^1$S) + $e_{pe}$ | $\sigma_2$ | | (3) |
| $e_{pe}$ + CO → O($^1$S) + C + $e_{pe}$ | $\sigma_3$ | | (4) |
| $O_2^+ + e_{th}$ → O + O($^1$S) | $\alpha_1$, | $QY_2 = 0.09$ | (5) |
| $CO_2^+ + e_{th}$ → CO + O($^1$S) | $\alpha_2$ | $QY_3 = 0.05$ | (6) |

### 4.2. Numerical Model

We first describe the model used to calculate the O($^1$S) vertical sources and density distribution including the relevant cross sections and quantum

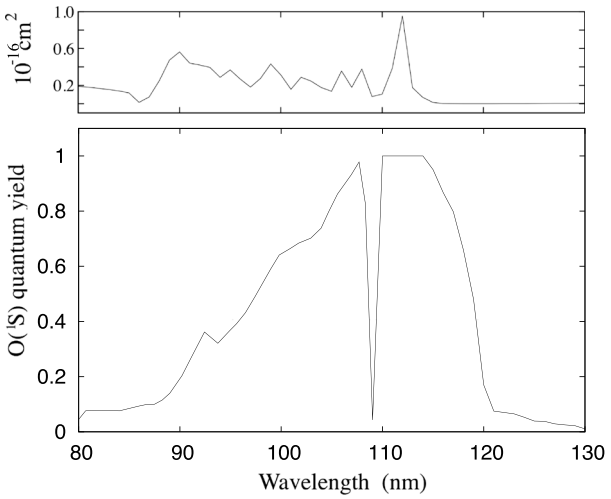


**Figure 5.** (top) $CO_2$ absorption cross section averaged in 1-nm bins applied in the calculation of the photodissociation rate. (bottom) Quantum yield for production of O($^1$S) atoms by photodissociation of $CO_2$ used in the airglow model (process 1; Table 1).

efficiencies; we then compare with earlier models and present sensitivity tests.

#### 4.2.1. Model Description

The steady state O($^1$S) density profile may be calculated in photochemical equilibrium, an assumption justified by the short (~0.8 s) effective lifetime of the metastable state. Three categories of sources of the excited state may be distinguished: photodissociation of $CO_2$ (process 1; Table 1), collisional excitation (processes 2 to 4), and chemical reactions (processes 5 and 6). Fox and Dalgarno (1979) showed that photodissociation is the dominant source at all altitudes below 250 km. The energy threshold for $CO_2$ dissociation is 5.45 eV (227-nm photons), but at least 9.84 eV (128.6 nm) are required to yield O atoms in the $^1$S state. At energies above 13.79 eV (89.9 nm), the molecule may be ionized and the efficiency for the production of O($^1$S) decreases with increasing photon energy. Therefore, in addition to the $CO_2$ density profile, three quantities are required to calculate the O($^1$S) production rate: the extreme ultraviolet (EUV) solar flux at Mars orbit at the time of the observations, the $CO_2$ absorption cross section and the quantum efficiency of the $^1$S state production as a function of wavelength.

The EUV solar flux is monitored by the Extreme Ultraviolet Monitor onboard MAVEN (Eparvier et al., 2015). It measures the solar irradiance in three wavelength ranges: 0–7, 17–22, and 117–125 nm. The full EUV spectrum is reconstructed, driven by the three Extreme Ultraviolet Monitor measurements, following the method described by Thiemann et al. (2017). It is based on the linear association of the broadband EUV measurements with spectral irradiance measurements. Calibrated solar spectra with a resolution of 1 nm obtained every minute are available from NASA's Planetary Data System website. The absolute calibration uncertainty at Lyman-α is estimated to be on the order of 5%. The availability of these direct measurements is a major advantage compared to previous Martian airglow studies based on terrestrial activity indices as it makes corrections for solar activity and Sun-Mars distance obsolete.

High-resolution measurements of the $CO_2$ absorption cross sections have recently become available from various studies. We combine the values measured by Gallagher et al. (1988) from 15 to 100 nm, Shaw et al. (1995) from 34.5 to the 89.9 nm, Archer et al. (2013) from 87 to 110 nm, Venot et al. (2018) from 114 to 185 nm, Stark et al. (2007) from 106 to 118 nm, Yoshino et al. (1996) from 118 to 175 nm, and Parkinson et al. (2003) from 163 to 200 nm to cover the range of ultraviolet absorption by $CO_2$. These values smoothly overlap and no scaling was necessary. The applied cross section is averaged over 1-nm intervals with the exception of the Lyman-α line profile (Figure 5, top panel). We adopt the line profile measured with the SUMER/SOHO high-resolution spectrometer by Lemaire et al. (1998) and scale it by the integrated flux value measured with the EUV instrument. The weighted average cross section is $6.54 \times 10^{-20}$ cm$^2$. Venot et al. (2018) investigated the dependence of this cross section with temperature. Their results indicate that it only drops by about 3% at 121.6 nm between 150 and 230 K, but they do not provide values below 150 K. Temperatures measured by stellar occultation in the 70–80-km region mostly range between 130 and 170 K, depending on the solar longitude (see for example Figure 8a of the study by Forget et al., 2009). The temperatures at the lower peak altitudes according to the Laboratoire de Météorologie Dynamique (LMD) model are 142, 144, 145, and 145 K for cases (a), (b), (c), and (d), respectively. The trend of the observed temperature dependence suggests that the cross section probably does not substantially vary in the temperature range of interest here. The uncertainty of the cross section is ±5% (Venot et al., private communication). Propagation of this uncertainty into our model corresponds to a ±0.4-km uncertainty in the altitude determination of the lower peak and a 8% uncertainty in the $CO_2$ density scaling factor.

The quantum yield of O($^1$S) atoms by process (1) is wavelength dependent and has not been measured recently. The first laboratory measurement by Lawrence (1972) indicated that it reaches about 100% between 110 and 114.2 nm and decreases at longer and shorter wavelengths. The measured value at Lyman-α was 13 $\pm^{2}_{8}$ %. The large uncertainty was caused by the very low value of the $CO_2$ absorption cross section at 121.6 nm which make measurements at this wavelength difficult. Further laboratory measurements have been

performed between 1979 and 1997 and summarized by Huestis et al. (2010). Figure 5 (bottom panel) shows the adopted values of the $QY_1$ photodissociation quantum yield. It is based on the recommended wavelength dependence by Huestis et al. (2010) above 108 nm and the laboratory measurements by Lawrence (1972) below this wavelength. As will be shown below, the best fit with the observed limb intensity is obtained for QY1 = 7.5%.

The contribution of photodissociation of $CO_2$ to the $O(^1S)$ production at altitude $z$ may then written as a sum of two terms:

$$\eta(O^1S) = [CO_2]_z \left\{\sigma_{Ly-\alpha}\, QY_{Ly-\alpha}\, F_{Ly-\alpha}\, \exp(-\tau_{Ly-\alpha}/\cos\chi) + \Sigma_i\, \sigma_i\, QY_i\, (\lambda_i)\, F\, (\lambda_i)\, \exp(-\tau_i/\cos\chi)\right\} \quad (8)$$

with $[CO_2]_z$ as the carbon dioxide number density at altitude z; $F_{Ly\text{-}\alpha}$ and F ($\lambda_i$) as the solar Lyman-$\alpha$ and the binned EUV fluxes, respectively, both measured outside the atmosphere; $\sigma_{Ly\text{-}\alpha}$ as the $CO_2$ photodissociation cross section at Lyman-$\alpha$; $\sigma_I$ as the photodissociation cross section in wavelength interval i; $\tau_{Ly\text{-}\alpha}$ as the vertical optical depth above altitude z for $CO_2$ absorption at Lyman-$\alpha$; $\tau_I$ as the vertical optical depth above altitude z in wavelength interval i; and $\chi$ as the solar zenith angle.In each wavelength interval i, $\tau_i$ is equal to $N_z$ ($CO_2$) $\sigma$ ($\lambda_i$).

Evaluation of collisional sources (2), (3), and (4) requires the calculation of the photoelectron spectrum as a function of altitude. The energy distribution function of the photoelectrons is obtained from the direct Monte Carlo simulation method that has a stochastic implementation of the Boltzmann equation for electron transport. The model has been developed for the atmospheres of the Earth, giant planets, Mars, and Venus. The description of the stochastic algorithmic implementation was given by Shematovich et al. (1994), and the application to the Martian dayglow and aurora was described by Gérard et al. (2008), Shematovich et al. (2008), Soret et al. (2016), and Gérard et al. (2017). The $O(^1S)$ excitation cross sections $\sigma_1$, $\sigma_2$, and $\sigma_3$ for electron impact on O, $CO_2$, and CO were described in Gérard et al. (2017).

Dissociative recombination of $O_2^+$ ions (process 5):

$$O_2^+ + e \rightarrow O + O(^1S)$$

is also a source of OI 297.2-nm excitation. The $O_2^+$ density is assumed to be in photochemical equilibrium below 200 km. Its density distribution is calculated using conventional Martian ion chemistry (Fox & Sung, 2001). In short, the production rate of $CO_2^+$ ions, P ($CO_2^+$), is obtained by combining photoionization of $CO_2$ (Gallagher et al., 1988) and photoelectron impact ionization of $CO_2$ (Itikawa, 2002). In the conventional Martian ionospheric photochemistry, the main source of $O_2^+$ ions in the lower thermosphere is the reaction of $CO_2^+$ with atomic oxygen $CO_2^+ + O \rightarrow O_2^+ + CO$. We assume that the loss of $O_2^+$ by dissociative recombination is balanced by the production resulting from this reaction. Fox et al. (2017) recently questioned the validity of this assumption on the basis of recent ion density measurements with the Neutral Gas and Ion Mass Spectrometer instrument onboard MAVEN and on new measurements of the coefficient rate (Tenewitz et al., 2018). They concluded that the $O^+ + CO_2$ reaction may be the dominant source of $O_2^+$ ions.

Following the laboratory work by Tenewitz et al. (2018) in order to examine the scenario suggesting that the $O^+ + CO_2$ reaction is the dominant source of $O_2^+$ ions, we have calculated this contribution in the lower emission peak. To do this, we used the $O^+$ density profile from the work by Fox et al. (1995). Below 90 km we used an upper limit for the $O^+$ density equal to $10^{-1}$ to $10^{-2}$ $cm^3$. In this case, the production of $O_2^+$ ions will be 100 to 10 times higher than in the (so far) conventional chemistry. In this case, the contribution to the total production of the $O(^1S)$ atoms will range between 0.01 and 0.3%. Therefore, even in this scenario we can firmly state that $CO_2$ photodissociation by Lyman-alpha is the main source and other ones are negligible. $O^+$ ions in the Martian lower thermosphere are produced by direct ionization of O atoms or $CO_2$ dissociative ionization producing $O^+ + CO$. Both of these processes require EUV solar photons or energetic photoelectrons. The unit optical depth for EUV photons with energy above 13.1 eV is reached at altitudes significantly higher than the OI 297.2-nm lower peak. Therefore, the production of $O^+$ ions and their density is vanishingly small below about 100 km.

However, until the revised value of this coefficient is confirmed, we use the conventional chemistry that provided good agreement with past measurements of the ion and electron density profiles. Since $O_2^+$ is the dominant ion in the dayside thermosphere, its density at photochemical equilibrium is then given in good

**Table 2**
*Parameters of the Groups of Limb Profiles in Figure 3*

| Parameter | (a) | (b) | (c) | (d) |
|---|---|---|---|---|
| $L_s$ (deg) | 50–80 | 135–145 | 350–360 | 215–230 |
| Latitude (deg) | 0–25 | 25–35 | 0–10 | 0–20 |
| SZA (deg) | 27.4 ± 5.5 | 15.2 ± 0.5 | 25.0 ± 3.1 | 36.5 ± 2.5 |
| Dates (month/year) | 10/2015–11/2015 | 4/2016–5/2016 | 4/2017–5/2017 | 10/2014–11/2014 |
| Range of orbits | 2018–2150 | 2973–2999 | 4933–5032 | 109–128 |
| Number of limb scans | 112 | 57 | 50 | 72 |
| Peak altitude (km) | 76.0 ± 1 | 78.0 ± 0.9 | 81.0 ± 0.8 | 89.0 ± 0.8 |
| $CO_2$ scaling factor | 0.50 (0.48[a]) | 0.45 | 0.62 | 0.66 |
| N $(CO_2)_{zmax}$ ($10^{19}$ $cm^2$) | 2.3 ± 0.3 | 2.3 ± 0.2 | 2.2 ± 0.2 | 2.1 ± 0.1 |
| N $(CO_2)_{slant}$ ($10^{19}$ $cm^2$) | 2.6 ± 0.3 | 2.4 ± 0.2 | 2.4 ± 0.2 | 2.6 ± 0.1 |

[a]Scaling factor for the density measurements made during the Viking 1 descent.

approximation by the balance between production of $O_2^+$ ions and loss by dissociative recombination, equal to ~$\alpha_{O2+}[O_2^+]^2$. The dissociative recombination coefficient $\alpha_{O2}^+$ is taken equal to $1.95 \times 10^{-7}$ (300/Te)$^{0.7}$ $cm^3/s$ (Alge et al., 1983). The calculated value for the Viking 1 descent below 200 km is in close agreement with the measured $O_2^+$ density profile. $CO_2$ photodissociation is by very far (>99.9%) the dominant source of O($^1$S) atoms in the lower thermosphere; therefore, a change in the $O_2^+$ density relative to the "conventional" photochemistry has no effect on the total production rate. We also note the photochemistry using the larger rate coefficient for the $O^+ + CO_2$ reaction leads to estimates of the O density by a factor of about 4 larger than the direct measurements from the Neutral Gas and Ion Mass Spectrometer below 155 km as indicated by Fox et al. (2017). This discrepancy suggests that uncertainties still exist in this question. In any case, as will be shown, dissociative recombination of $O_2^+$ ions is a very minor source of O($^1$S) atoms in the region of the lower emission peak.

To evaluate the relative importance of dissociative recombination of $O_2^+$ recombination as a source of O($^1$S) atoms, we use in a first step the measured Viking $O_2^+$ density profile, the only measurement covering the altitude range needed for this study (Fehsenfeld et al., 1970) Its contribution to the production rate is then given by

$$\eta(O^1S) = \alpha_{O2+}\, QY_2\, [O_2^+]^2 = QY_2\, P(O_2^+) \quad (9)$$

The quantum yield $QY_2$ for O($^1$S) production from $O_2^+$ recombination depends on the vibrational excitation of the oxygen ions (Kella et al., 1997). Larger values have been obtained if the ions are vibrationally excited. In this study, following Fox and Hać (2009), we assume that most ions are in the vibrational ground state and use a yield of 9%, the value measured in the laboratory for $O_2^+$ ions in their vibrational ground state. The vertical distribution of the electron temperature is based on the dayside profile calculated by Fox and Sung (2001). A minor contribution of about 0.1% is also provided by process (6). We use a recombination coefficient $\alpha_2 = 4.2 \times 10^{-7}$ (300/Te)$^{0.7}$ (Viggiano et al., 2005), with an O($^1$S) quantum yield $QY_3 = 0.05$.

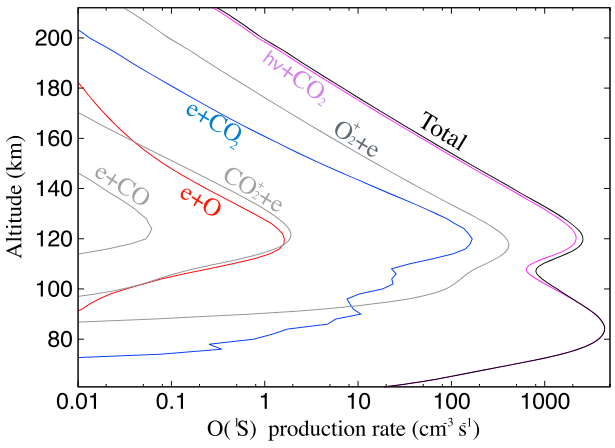


**Figure 6.** Volume production rate of O($^1$S) calculated for the conditions of the Viking 1 descent.

The temperature and densities of the major neutral constituents are obtained from the Mars Climate Data, version 5.3, that provides simulations from the Laboratoire de Météorologie Dynamique (LMD) model (Forget et al., 1999; Gonzalez-Galindo et al., 2009; Millour et al., 2015) for the selection of Martian latitude, season, local time, and solar activity conditions given in Table 2 for cases (b) to (d) while we use Viking 1 in situ measurements for case (a). In the following examples, the temperature and density vertical distributions were calculated every kilometer between 50 and 200 km.

The relative importance of the various sources is shown as a function of altitude in Figure 6. The pressure, neutral, and electron temperature and

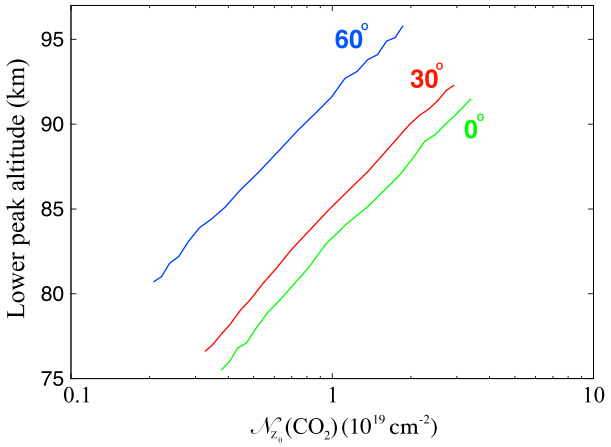


**Figure 7.** Dependence of the altitude of the peak O($^1$S) atom production rate versus the $CO_2$ column density overlying the reference altitude for three values of the solar zenith angle.

the $CO_2$, O, and CO densities used in these calculations were given by Fox and Hać (2009). They correspond to the conditions prevailing during the descent of the Viking 1 lander as measured with the onboard mass spectrometer (22°N latitude, $L_s$ = 98°, local time = 16:13, SZA = 44°) so that the evaluation of the importance of the source processes is rooted in the only in situ measurements available so far. As mentioned before, in this example we also adopt the $O_2^+$ density profile measured with the retarding potential analyzer onboard Viking 1. In this way, the contribution of process (2) is directly calculated based on ion density measurements and is consistent with the vertical distribution of the neutral constituents measured in situ simultaneously. The comparison shows that photodissociation of $CO_2$ by solar Lyman-α and EUV radiation (process 1) is by far dominant at all altitudes below 200 km. It contributes 86% of the production rate at the upper peak while contributions from all other sources are negligible at the lower altitude peak. Simulations for other seasons and solar activity conditions have shown that, in all cases, photodissociation totally dominates over all other sources by about the same factor. The second most important source is $O_2^+$ recombination, followed by electron impact dissociation of $CO_2$. Other sources contribute less than 1% of the total.

These results lead to the conclusion that only process (1) controls the altitude of the OI 297.2-nm emission peaks. This point will be developed further below and used to demonstrate that the altitude of the emission peak may be used as a proxy for the $CO_2$ column density overlying the peak altitude and thus the pressure level. For comparison with IUVS limb observations, the calculated volume emission rate is numerically integrated along the line of sight.

#### 4.2.2. Comparison With Earlier Models

The presence of a second lower altitude peak of the OI 297.2-nm emission was predicted by earlier models of the O($^1$S) density distribution. Fox and Dalgarno (1979) presented calculations of the volume emission rate showing a lower peak of both 557.7 nm and MUV emissions from O($^1$S) atoms. The emission reached a maximum at ~85 km, a value within the range of the IUVS results summarized in Table 2. Their ratio of the brightness of the lower peak relative to the upper peak located at 125 km was ~2.2, also in agreement with the four IUVS measured ratios ranging between 1.7 and 2.2 and our model values ranging from 2 to 2.2. Gronoff et al. (2012) also calculated the production rate of O($^1$S) atoms, including the lower peak. They obtained a maximum near 88 km, but they predicted an upper peak intensity approximately 1.5 times larger than the lower one for the $CO_2$ dissociation source alone and over a factor of 2 when all sources are included, in contradiction with the IUVS observations. Finally, Jain (PhD thesis, 2013) obtained O($^1$S) production peaks at 96 and 138 km for solar maximum conditions and 88 and 132 km for solar minimum. The ratio of the production rate at the two peaks was ~2.5 for both solar maximum and minimum. The differences between the models probably stem from improvements of the $CO_2$ absorption and photodissociation cross sections, solar Lyman-α intensity at Mars orbit, and use of different neutral atmospheric structures. In any case, our model makes use of the latest available molecular and atomic data and in orbit measurements of the solar EUV and Lyman-α solar fluxes.

#### 4.2.3. Sensitivity of the O($^1$S) Production

In this section we present sensitivity tests on the dependence of the column density at a $Z_0$, reference altitude, with the change of the production peak altitude $Z_{max}$. Figure 7 illustrates the dependence of the altitude of the maximum O($^1$S) production rate calculated with the full model as a function of the vertical $CO_2$ column density N ($CO_2$) overlying a reference altitude for three values of the solar zenith angle χ. In this case, the reference altitude $z_0$ is taken as equal to 83.5 km, the peak altitude calculated for a 0° solar zenith angle. The plot shows that the altitude of the lower peak production varies quasi-linearly with the logarithm of the $CO_2$ column density at a fixed altitude. The small departures from straight lines are caused by the rounding error at the closest kilometer. The lines run quasi-parallel to each other, implying a close relationship between the scaling factor of the $CO_2$ column and the linear change of the peak altitude. In a first approximation, a doubling of the $CO_2$ column leads to an increase of the emission

maximum by ~5 km (Evans et al., 2015). As an example, the least squares linear fit to the (green) curve for a 0° solar zenith angle is given by

$$Z_{max} = 16.63\ \log_{10}\left[N_{Z0}\ (CO_2)\right] - 233.2 \tag{10}$$

where $Z_{max}$ is in km and $N_{Z0}$ $(CO_2)$ in $cm^2$.

It is interesting to note that the production rate of $O(^1S)$ in the lower peak is closely described by a Chapman layer since one solar UV emission (Lyman-α) essentially produces the layer and only one constituent ($CO_2$) is both the source of metastable atoms and the sole Lyman-α absorber. Only the assumption of isothermal vertical profile is not strictly verified in this case. In the Chapman layer approach, the altitude $z_{max}$ of the maximum production rate is given by the condition that the slant optical depth is equal to unity, expressed as

$$N\ (CO_2)_{zmax} = \cos\chi/\sigma_{Ly-\alpha} = 1.53\times10^{19}\ \cos\chi\ cm^2 \tag{11}$$

which leads to the expression

$$z_{max} = Z_0 + H\ \ln\left(\left[CO_2\right]_z\ \sigma_{Ly-\alpha}\ H/\cos\chi\right), \tag{12}$$

where N $(CO_2)$ is the vertical overhead column of $CO_2$, H is the $CO_2$ scale height, $\sigma_{Ly\text{-}\alpha}$ is the $CO_2$ absorption cross section at Lyman-α, χ is the solar zenith angle, and $[CO_2]_{z0}$ is the $CO_2$ density at a fixed reference altitude $z_0$. We note that, for a constant value of H, $z_{max}$ is expected to vary linearly with the logarithm of the $CO_2$ column density at the reference altitude, in agreement with the results shown in Figure 7. Comparisons indicate that the maximum production rate calculated with the full model is in close agreement with the value given by equation (12). For negligible quenching, it will also correspond to the maximum $O(^1S)$ atom density and 297.2-nm volume emission rate from $O(^1S)$. In this case, the slant $CO_2$ column density at the production peak will be equal to $1.53 \times 10^{19}/\cos\chi\ cm^2$. Accounting for the presence of $N_2$ and Ar, the ratio of the total gas column above the lower emission peak to the $CO_2$ column is equal to 1.04, for a $CO_2$ mixing ratio of 0.96. Consequently, the pressure levels corresponding to unit optical depth are 43.2, 37.4, and 21.6 nbars for solar zenith angles of 0°, 30°, and 60°, respectively. This is an important result as it provides a tool to remotely sense the $CO_2$ column density above the emission peak and the altitude of the corresponding pressure level.

## 5. Comparison of Modeled and Observed Limb Profiles

We now compare three sets of observed limb profiles collected with the IUVS instrument at different seasons, latitudes, and solar zenith angles with our model simulations for the same average conditions (Table 2). The atmospheric composition, pressure, and temperature dependence on altitude are based on the values provided by the Mars Climate Model Database (MCD) for the corresponding place and time as the IUVS observations. Since the altitude is directly controlled by the amount of $CO_2$ molecules irradiated by Lyman-α and the brightness by the uncertain $QY_{Ly\text{-}alpha}$ quantum yield, the two quantities may be determined independently. We thus multiply the $CO_2$ column density provided by the Mars Climate Model by a scaling factor so that the lower emission peak matches the observed altitude within less than 1 km. For this purpose, a quadratic function is calculated by a least squares Levenberg–Marquardt fit to the highest-intensity points within ±20 km of the peak and shown as a dashed black curve in Figure 3. The uncertainty on the lower peak altitude is obtained by propagating the error on the coefficients of the quadratic fit combined with the statistical uncertainty on the altitude of the tangent point. The altitude of the maximum emission in the four quadratic fits is then determined with an error less than ±1 km. This altitude uncertainty is then converted into uncertainties on the slant and vertical $CO_2$ columns. In the Table, N $(CO_2)_{zmax}$ is the model $CO_2$ vertical column density overlying the altitude level of maximum $O(^1S)$ production and N $(CO_2)_{slant}$ the slant column density over this altitude level. These values are determined with an uncertainty between 5 and 10%. The $QY_{Ly\text{-}\alpha}$ quantum yield factor in expression (9) is adjusted to best match the observed peak intensities. We determined that a $QY_{Ly\text{-}\alpha}$ efficiency of (7.5 ± 2.5)% provides the best global fit to the set of modeled limb profiles. The comparisons are shown in Figure 3, together with the peak altitude.

The first case (Figure 3a) is the closest to the Viking 1 conditions that were used before as a model case in section 4 and Figures 6 and 7. However, no IUVS observations were made at the same season, so that solar longitudes were ~40° less than during the Viking 1 descent. We adopt the MCD model atmosphere for

latitude and solar zenith angle conditions appropriate for the IUVS observations. The IUVS measurements cover a two-month period in 2015. The corresponding MCD neutral atmosphere was combined with direct Extreme Ultraviolet Monitor measurements and solar spectrum concurrent with the IUVS observations. For comparison and increased accuracy in the determination of the observed emission peak, a quadratic curve was fitted to the IUVS observations as explained before. The best fit to the measured altitude of the lower peak was obtained by scaling the MCD $CO_2$ density profile by a factor of 0.50. The calculated intensity above 120 km is also in reasonably good agreement with the IUVS measurements, although the production of O($^1$S) between 100 and 120 km is somewhat underestimated. Most of these discrepancies likely stem from the lack of simultaneity between the neutral atmospheric structure of the MCD model and the IUVS observations.

The densities and temperature measured during the Viking descent have been extensively used in the literature and used in this study to compare the O($^1$S) sources. Therefore, we also calculated the emission profile and the density scaling factor to best match the observed peak altitude. In this case, we found $N(CO_2)_{zmax} = 2.5 \times 10^{19}$ cm$^2$ and $N(CO_2)_{slant} = 2.8 \times 10^{19}$ cm$^2$. The scaling factor for the $CO_2$ column was then equal to 0.38. In the other three cases (Figures 3b–3d), the average limb profiles were measured at different latitudes, seasons, and solar zenith angles as shown in Table 2. The table also lists the observed lower peak altitude and $CO_2$ column scaling factors relative to the MCD model providing the best match with the observations. The atmospheric model corresponds to the average locations, season, and solar activity of the IUVS observations. The scaling factors applied to the MCD total density to match the observed emission peak altitude ±0.5 km were 0.45, 0.62, and 0.66. The ratio of the lower to upper peak intensity is well reproduced by the model, but the calculated maximum intensity of both peaks in Figure 3d are too small by about 10 and 25% for the lower and upper peaks, respectively. We also note that the slant column density $N(CO_2)_{slant}$ over the lower emission peak is within the range $2.5 \pm 0.1 \times 10^{19}$ cm$^2$. As expected, this value is larger than $1.53 \times 10^{19}/\cos\chi$ cm$^2$, the column for unit optical depth at Lyman-$\alpha$ given in equation (12). This difference stems from the fact that the line of sight integration of the 297.2-nm emission peaks at a tangent point altitude located a fraction of a scale height below the peak of the production of O($^1$S) atoms. The altitude of the upper peak is also well reproduced by the model in all four cases, but the slopes above 120 km are somewhat steeper than in the dayglow observations. This suggests that the temperature profiles in the MCD atmospheric model may be different from the actual temperature gradient in this region.

## 6. Discussion

The results presented in section 4 confirm the presence of two peaks in the O($^1$S) emission profile in the Martian atmosphere as was first suggested by Fox and Dalgarno in 1979, about 35 years before the lower emission peak was detected. Comparison with our model confirms that photodissociation of $CO_2$ is the major source of O($^1$S) atoms below 200 km and the dominant excitation process of the lower peak. Simulations have also indicated that there is no correlation between the upper emission peak and the altitude and the intensity of the lower peak based on MAVEN/IUVS observations. A direct consequence is that the altitude of the lower peak of 297.2-nm emission is solely controlled by the overlying column density of $CO_2$, while the maximum brightness depends essentially on the solar Lyman-$\alpha$ line intensity. The agreement with the model calculations is generally not as good for the upper emission peak for several reasons. Although $CO_2$ photodissociation remains the dominant excitation process, other sources such as photoelectron impact and $O_2^+$ recombination still play a role in the control of the altitude and intensity of the upper peak. In addition, the MCD model used for the neutral densities and temperature appear to produce a slope of the emission that is too steep above 120 km relative to the observations as evidenced in Figures 3b–3d. A future systematic study of the intensity gradient above the lower peak and comparisons between modeled and measured temperature gradient above 100 km should clarify this issue.

The brightness of the lower peak linearly depends on the quantum efficiency of process (1) in the vicinity of 121.6 nm. Its value is derived here by adjusting the QY1 quantum yield for O($^1$S). The best agreement with the observations in the four cases illustrated in this study is obtained for QY1 equal to 7.5 ± 0.1%, a value on the lower side of uncertainty of the measurement by Lawrence (1972) at this wavelength. The determination of this value depends linearly on the brightness calibration of the IUVS instrument. Additionally, if later studies establish that the branching ratio between the 557.7- and 297.2-nm emissions is close to 9.5 instead of ~15 as measured in the airglow/aurora, then the value of the QY1 quantum efficiency would need to be revised up

by a factor of about 1.6 This value would still be within the range of uncertainties provided by the Lawrence (1972) laboratory measurement.

Since the altitude of the lower peak directly depends on the $CO_2$ column illuminated by the solar radiation, its value may be used as an indicator of the seasonal/latitudinal variations of the thermospheric $CO_2$ distribution and therefore of the changes of altitude of the $\tau = 1$ level. These altitude changes correspond to variations of the altitude of the isobars that are controlled by the seasonal pressure variations and the lower atmosphere dust load. As may be noticed in Table 2, the scaling factor of the $CO_2$ column density is less than unity in all four analyzed cases. This result implies that the $CO_2$ density in the region above the lower peak altitude is less than predicted by the LMD model by a factor between 0.45 and 0.66 for cases (b), (c) and (d). For case (a), we use the density measured in situ during the Viking 1 descent, but the IUVS measurements were made 42 years later at a different solar activity level and higher solar longitudes. The scaling factor providing the best fit to the emission peak altitude is 0.38 in this case. Discrepancies with the $CO_2$ density values calculated with the LMD model was previously noticed by Forget et al. (2009) when they compared the nightside $CO_2$ density profiles deduced using the SPICAM stellar occultation technique with those calculated with the LMD model for the same conditions. The latter were generally overestimated between 70 and 100 km, sometimes by a factor exceeding 2. They also concluded that difference stemmed from the temperature profile predicted by the LMD GCM between 85 and 100 km.

## 7. Conclusions and Summary

Observations of the oxygen $^1S$-$^3P$ limb airglow emission in the dayside Martian thermosphere at 297.2 nm confirm earlier model predictions that it is characterized by two peaks, one between 70 and 90 km and a second one near 120 km. Comparison with model calculations including all important sources of $O(^1S)$ atoms indicates that the production of $O(^1S)$ is dominated by photodissociation of $CO_2$ and does not reflect the $O(^3P)$ content of the upper atmosphere. Therefore, the intensity distribution only depends on the Lyman-$\alpha$ and EUV solar fluxes and the vertical distribution of $CO_2$. Our model simulations are based on most recent high spectral resolution $CO_2$ absorption cross sections. We also take advantage of the direct measurements of the Lyman-$\alpha$ intensity at Mars' distance from the Sun onboard MAVEN and the reconstructed EUV solar spectrum to significantly reduce a source of uncertainty in the model calculations. The $O(^1S)$ sources other than photodissociation are calculated from photochemical processes such as photoelectron impact, which are also controlled by the EUV solar spectrum. A full Monte Carlo model is used to determine the photoelectron energy spectrum as a function of altitude. These energy spectra have then been folded with the relevant cross section to calculate the total emission rate as a function of altitude. Our calculations indicate that, in the altitude range where the 297.2-nm dayglow is observed, collisional quenching only plays a minor role. We also determine that the relatively unknown quantum yield for $O(^1S)$ atom production for $CO_2$ photodissociation by Lyman-$\alpha$ wavelength is about 8% if the branching ratio between this emission and the oxygen green line matches the value given by ab initio calculations. The same quantum yield was used in the pioneering work by Fox and Dalgarno (1979), decades before the lower emission peak was detected. By minimizing the sources of uncertainties in the model calculations, the comparison between the limb profiles observed with IUVS and the model simulations make it possible to constrain the overlying column of $CO_2$, a quantity directly related to the atmospheric pressure.

In future studies, we will use this emission and its variations as a tool to remotely sense the changes in altitude of the critical level where the lower emission peak is formed. First comparisons with $CO_2$ column densities calculated with the LMD GCM (available from Mars Climate Database at http://www-mars.lmd.jussieu.fr/mars/access.html) suggest that the model values are overestimated by a factor of 2 or more. Earlier comparisons with other remote sensing methods lead to similar conclusions.

**Acknowledgments**
This research was partly funded by the NOMAD PRODEX program managed by the European Space Agency with the help of the Belgian Science Policy Office (BELSPO) and by BELSPO's SCOOP/BRAIN research contract. B.H. is supported by the Belgian Fund for Scientific Research (FNRS). The IUVS and EUVM MAVEN data sets were obtained from NASA's Planetary Data System (PDS) available at http://atmos.nmsu.edu/data_and_services/atmospheres_data/MAVEN/maven_main.html. The IUVS archive levels V07 and V12 for the orbits 5680–6073 were used for this study. The Mars Climate Database (version 5.3) is available online at http://www-mars.lmd.jussieu.fr/mars/access.html.

## References

Alge, E., Adams, N. G., & Smith, D. (1983). Measurements of the dissociative recombination coefficients of $O_2^+$, $NO^+$ and $NH_4^+$ in the temperature range 200–600 K. *Journal of Physics B: Atomic and Molecular Physics*, *16*(8), 1433–1444. https://doi.org/10.1088/0022-3700/16/8/017

Archer, L. E., Stark, G., Smith, P. L., Lyons, J. R., de Oliveira, N., Nahon, L., et al. (2013). Room temperature photoabsorption cross section measurements of $CO_2$ between 91,000 and 115,000 $cm^{-1}$. *Journal of Quantitative Spectroscopy and Radiative Transfer*, *117*, 88–92. https://doi.org/10.1016/j.jqsrt.2012.11.009

Barth, C. A., Hord, C. W., Pearce, J. B., Kelly, K. K., Anderson, G. P., & Stewart, A. I. (1971). Mariner 6 and 7 ultraviolet spectrometer experiment: Upper atmosphere data. *Journal of Geophysical Research*, *76*(10), 2213–2227. https://doi.org/10.1029/JA076i010p02213

Barth, C. A., Stewart, A. I., Hord, C. W., & Lane, A. L. (1972). Mariner 9 ultraviolet spectrometer experiment: Mars airglow spectroscopy and variations in Lyman alpha. *Icarus*, *17*(2), 457–468. https://doi.org/10.1016/0019-1035(72)90011-5

Capetanakis, F. P., Sondermann, F., Höser, S., & Stuhl, F. (1993). Temperature dependence of the quenching of $O(^1S)$ by simple inorganic molecules. *The Journal of Chemical Physics*, *98*(10), 7883–7887. https://doi.org/10.1063/1.464596

Chamberlain, T. P., & Hunten, D. M. (1990). *Theory of Planetary Atmospheres: An Introduction to Their Physics and Chemistry* (Vol. 36). New York: Academic Press.

Chantler, C. T., Nguyen, T. V. B., Lowe, J. A., & Grant, I. P. (2013). Relativistic calculation of transition probabilities for 557.7 nm and 297.2 nm emission lines in oxygen. *The Astrophysical Journal*, *769*(1), 84. https://doi.org/10.1088/0004-637X/769/1/84

Eparvier, F. G., Chamberlin, P. C., Woods, T. N., & Thiemann, E. M. B. (2015). The solar Extreme Ultraviolet Monitor for MAVEN. *Space Science Reviews*, *195*(1–4), 293–301. https://doi.org/10.1007/s11214-015-0195-2

Evans, J. S., Stevens, M. H., Lumpe, J. D., Schneider, N. M., Stewart, A. I. F., Deighan, J., et al. (2015). Retrieval of $CO_2$ and $N_2$ in the Martian thermosphere using dayglow observ ations by IUVS on MAVEN. *Geophysical Research Letters*, *42*, 9040–9049. https://doi.org/10.1002/2015GL065489

Fehsenfeld, F. C., Dunkin, D. B., & Ferguson, E. E. (1970). Rate constants for the reaction of $CO_2^+$ with O, $O_2$ and NO; $N_2^+$ with O and NO; and $O_2^+$ with NO. *Planetary and Space Science*, *18*(8), 1267–1269. https://doi.org/10.1016/0032-0633(70)90216-3

Fischer, C. F., & Tachiev, G. (2004). Breit–Pauli energy levels, lifetimes, and transition probabilities for the beryllium-like to neon-like sequences. *Atomic Data and Nuclear Data Tables*, *87*(1), 1–184. https://doi.org/10.1016/j.adt.2004.02.001

Forget, F., Hourdin, F., Fournier, R., Hourdin, C., Talagrand, O., Collins, M., et al. (1999). Improved general circulation models of the Martian atmosphere from the surface to above 80 km. *Journal of Geophysical Research*, *104*(E10), 24,155–24,175. https://doi.org/10.1029/1999JE001025

Forget, F., Montmessin, F., Bertaux, J. L., González-Galindo, F., Lebonnois, S., Quemerais, E., et al. (2009). Density and temperatures of the upper Martian atmosphere measured by stellar occultations with Mars express SPICAM. *Journal of Geophysical Research*, *114*, E01004. https://doi.org/10.1029/2008JE003086

Fox, J. L., & Dalgarno, A. (1979). Ionization, luminosity, and heating of the upper atmosphere of Mars. *Journal of Geophysical Research*, *84*(A12), 7315–7333. https://doi.org/10.1029/JA084iA12p07315

Fox, J. L., & Hać, A. B. (2009). Photochemical escape of oxygen from Mars: A comparison of the exobase approximation to a Monte Carlo method. *Icarus*, *204*(2), 527–544. https://doi.org/10.1016/j.icarus.2009.07.005

Fox, J. L., Johnson, A. S., Ard, S. G., Shuman, N. S., & Viggiano, A. A. (2017). Photochemical determination of O densities in the Martian thermosphere: Effect of a revised rate coefficient. *Geophysical Research Letters*, *44*, 8099–8106. https://doi.org/10.1002/2017GL074562

Fox, J. L., & Sung, K. Y. (2001). Solar activity variations of the Venus thermosphere/ionosphere. *Journal of Geophysical Research*, *106*(A10), 21,305–21,335. https://doi.org/10.1029/2001JA000069

Fox, J., Zhou, P., & Bougher, S. (1995). The Martian thermosphere/ionosphere at high and low solar activities. *Advances in Space Research*, *17*(11), 203–218. https://doi.org/10.1016/0273-1177(95)00751-Y

Gallagher, J. W., Brion, C. E., Samson, J. A. R., & Langhoff, P. W. (1988). Absolute cross sections for molecular photoabsorption, partial photoionization, and ionic photofragmentation processes. *Journal of Physical and Chemical Reference Data*, *17*(1), 9–153. https://doi.org/10.1063/1.555821

Gattinger, R. L., Lloyd, N. D., Bourassa, A. E., Degenstein, D. A., McDade, I. C., & Llewellyn, E. J. (2009). Observation of the 557.7 nm to 297.2 nm brightness ratio in the auroral spectrum with OSIRIS on Odin. *Canadian Journal of Physics*, *87*(10), 1133–1137. https://doi.org/10.1139/P09-102

Gérard, J. C., Hubert, B., Shematovich, V. I., Bisikalo, D. V., & Gladstone, G. R. (2008). The Venus ultraviolet oxygen dayglow and aurora: model comparison with observations. *Planetary and Space Science*, *56*, 542–552. https://doi.org/10.1016/j.pss.2007.11.008

Gérard, J.-C., Soret, L., Shematovich, V. I., Bisikalo, D. V., & Bougher, S. W. (2017). The Mars diffuse aurora: A model of ultraviolet and visible emissions. *Icarus*, *288*, 284–294. https://doi.org/10.1016/j.icarus.2017.01.037

González-Galindo, F., Forget, F., López-Valverde, M. A., Angelats i Coll, M., & Millour, E. (2009). A ground-to-exosphere Martian general circulation model: 1. Seasonal, diurnal, and solar cycle variation of thermospheric temperatures. *Journal of Geophysical Research*, *114*, E04001. https://doi.org/10.1029/2008JE003246

Gronoff, G., Simon Wedlund, C., Mertens, C. J., Barthélemy, M., Lillis, R. J., & Witasse, O. (2012). Computing uncertainties in ionosphere-airglow models: II. The Martian airglow. *Journal of Geophysical Research*, *117*, A05309. https://doi.org/10.1029/2011JA017308

Hanson, W. B., Sanitani, S., & Zuccaro, D. R. (1977). The Martian ionosphere as observed by the Viking retarding potential analyzers. *Journal of Geophysical Research*, *82*, 4351–4363. https://doi.org/10.1029/JS082i028p04351

Huestis, D. L., Slanger, T. G., Sharpee, B. D., & Fox, J. L. (2010). Chemical origins of the Mars ultraviolet dayglow. *Faraday Discussions*, *147*, 307–322. https://doi.org/10.1039/c003456h

Itikawa, Y. (2002). Cross sections for electron collisions with carbon dioxide. *Journal of Physical and Chemical Reference Data*, *31*(3), 749–767. https://doi.org/10.1063/1.1481879

Jain, S. K. (2013). Dayglow emissions on Mars and Venus, Ph.D. Thesis, Cochin University of Science and Technology, India. https://dyuthi.cusat.ac.in/jspui/handle/purl/3688

Jain, S. K., Stewart, A. I. F., Schneider, N. M., Deighan, J., Stiepen, A., Evans, J. S., Stevens, M. H., et al. (2015). The structure and variability of Mars upper atmosphere as seen in MAVEN/IUVS dayglow observations. *Geophysical Research Letters*, *42*, 9023–9030. https://doi.org/10.1002/2015GL065419

Kella, D., Vejby-Christensen, L., Johnson, P. J., Pedersen, H. B., & Andersen, L. H. (1997). The source of green light emission determined from a heavy-ion storage ring experiment. *Science*, *276*(5318), 1530–1533. https://doi.org/10.1126/science.276.5318.1530

Kramida, A., Ralchenko, Yu., Reader, J., & NIST ASD Team (2018). NIST Atomic Spectra Database (ver. 5.5.6), [Online]. Available: https://physics.nist.gov/asd [2018, April 10]. National Institute of Standards and Technology, Gaithersburg, MD.

Krauss, M., & Neumann, D. (1975). On the interaction of $O(^1S)$ with $O(^3P)$. *Chemical Physics Letters*, *36*(3), 372–374. https://doi.org/10.1016/0009-2614(75)80259-4

Lawrence, G. M. (1972). Production of O ($^1S$) from photodissociation of $CO_2$. *The Journal of Chemical Physics*, *57*(12), 5616–5617. https://doi.org/10.1063/1.1678271

Leblanc, F., Chaufray, J. Y., Lilensten, J., Witasse, O., & Bertaux, J. L. (2006). Martian dayglow as seen by the SPICAM UV spectrograph on Mars express. *Journal of Geophysical Research*, *111*, E09S11. https://doi.org/10.1029/2005JE002664

Lemaire, P., Emerich, C., Curdt, W., Schühle, U., & Wilhelm, K. (1998). Solar HI Lyman alpha full disk profile obtained with the SUMER/SOHO spectrometer. *Astronomy and Astrophysics*, *334*, 1095–1098.

McClintock, W. E., Schneider, N. M., Holsclaw, G. M., Clarke, J. T., Hoskins, A. C., Stewart, I., et al. (2015). The Imaging Ultraviolet Spectrograph (IUVS) for the MAVEN mission. *Space Science Reviews*, *195*(1–4), 75–124. https://doi.org/10.1007/s11214-014-0098-7

Millour, E. Forget, F., Spiga, A., Navarro, T., Madeleine, J.-B., Montabone, L., et al. (2015). The Mars Climate Database (MCD version 5.2), EPSC abstract 2015–438, Vol. 10,

Nier, A. O., & McElroy, M. B. (1977). Composition and structure of Mars' Upper atmosphere: Results from the neutral mass spectrometers on Viking 1 and 2. *Journal of Geophysical Research*, *82*, 4341–4349. https://doi.org/10.1029/JS082i028p04341

Parkinson, W. H., Rufus, J., & Yoshino, K. (2003). Absolute absorption cross section measurements of $CO_2$ in the wavelength region 163–200 nm and the temperature dependence. *Chemical Physics*, *290*(2–3), 251–256. https://doi.org/10.1016/S0301-0104(03)00146-0

Schneider, N., Deighan, J. I., Stewart, A. I. F., McClintock, W. E., Jain, S. K., Chaffin, M. S., et al. (2015). MAVEN IUVS observations of the aftermath of the Comet Siding Spring meteor shower on Mars. *Geophysical Research Letters*, *42*, 4755–4761. https://doi.org/10.1002/2015GL063863

Shaw, D. A., Holland, D. M. P., Hayes, M. A., MacDonald, M. A., Hopkirk, A., & McSweeney, S. M. (1995). A study of the absolute photoabsorption, photoionisation and photodissociation cross sections and the photoionisation quantum efficiency of carbon dioxide from the ionisation threshold to 345 Å. *Chemical Physics*, *198*(3), 381–396. https://doi.org/10.1016/0301-0104(95)00159-L

Shematovich, V. I., Bisikalo, D. V., & Gérard, J.-C. (1994). A kinetic model of the formation of the hot oxygen geocorona: 1. Quiet geomagnetic conditions. *Journal of Geophysical Research*, *99*(A12), 23,217–23,228. https://doi.org/10.1029/94JA01769

Shematovich, V. I., Bisikalo, D. V., Gérard, J.-C., Cox, C., Bougher, S. W., & Leblanc, F. (2008). Monte Carlo model of electron transport for the calculation of Mars dayglow emissions. *Journal of Geophysical Research*, *113*, E02011. https://doi.org/10.1029/2007JE002938

Simon, C., Witasse, O., Leblanc, F., Gronoff, G., & Bertaux, J. L. (2009). Dayglow on Mars: Kinetic modelling with SPICAM UV limb data. *Planetary and Space Science*, *57*(8–9), 1008–1021. https://doi.org/10.1016/j.pss.2008.08.012

Slanger, T. G., & Black, G. (1981). Quenching of O ($^1$S) by $O_2$ ($a^1\Delta g$). *Geophysical Research Letters*, *8*(5), 535–538. https://doi.org/10.1029/GL008i005p00535

Slanger, T. G., Cosby, P. C., Sharpee, B. D., Minschwaner, K. R., & Siskind, D. E. (2006). O ($^1$S→ $^1$D, $^3$P) branching ratio as measured in the terrestrial nightglow. *Journal of Geophysical Research*, *111*, A12318. https://doi.org/10.1029/2006JA011972

Soret, L., Gérard, J.-C., Libert, L., Shematovich, V. I., Bisikalo, D. V., Stiepen, A., & Bertaux, J.-L. (2016). SPICAM observations and modeling of Mars aurorae. *Icarus*, *264*, 398–406. https://doi.org/10.1016/j.icarus.2015.09.023

Stark, G., Yoshino, K., Smith, P. L., & Ito, K. (2007). Photoabsorption cross section measurements of $CO_2$ between 106.1 and 118.7 nm at 295 and 195 K. *Journal of Quantitative Spectroscopy and Radiative Transfer*, *103*(1), 67–73. https://doi.org/10.1016/j.jqsrt.2006.07.001

Stevens, M. H., Evans, J. S., Schneider, N. M., Stewart, A. I. F., Deighan, J., Jain, S. K., et al. (2015). New observations of molecular nitrogen in the Martian upper atmosphere by IUVS on MAVEN. *Geophysical Research Letters*, *42*, 9050–9056. https://doi.org/10.1002/2015GL065319

Stewart, A. I. (1972). Mariner 6 and 7 ultraviolet spectrometer experiment: Implications of $CO_2^+$, CO and O airglow. *Journal of Geophysical Research*, *77*(1), 54–68. https://doi.org/10.1029/JA077i001p00054

Stewart, A. I., Barth, C. A., Hord, C. W., & Lane, A. L. (1972). Mariner 9 ultraviolet spectrometer experiment: Structure of Mars' upper atmosphere. *Icarus*, *17*(2), 469–474. https://doi.org/10.1016/0019-1035(72)90012-7

Tenewitz, J. E., Lê, T., Martinez, O. Jr., Ard, S. G., Shuman, N. S., Sanchez, J. C., et al. (2018). Kinetics of $CO^+$ and $CO_2^+$ with N and O atoms. *The Journal of Chemical Physics*, *148*(8), 084305. https://doi.org/10.1063/1.5011195

Thiemann, E., Chamberlin, P. C., Eparvier, F. G., Templeman, B., Woods, T. N., Bougher, S. W., & Jakosky, B. M. (2017). The MAVEN EUVM model of solar spectral irradiance variability at Mars: Algorithms and results. *Journal of Geophysical Research: Space Physics*, *122*, 2748–2767. https://doi.org/10.1002/2016JA023512

Venot, O., Bénilan, Y., Fray, N., Gazeau, M. C., Lefèvre, F., Es-sebbar, E., et al. (2018). VUV-absorption cross section of carbon dioxide from 150 to 800 K and applications to warm exoplanetary atmospheres. *Astronomy & Astrophysics*, *609*, A34. https://doi.org/10.1051/0004-6361/201731295

Viggiano, A. A., Ehlerding, A., Hellberg, F., Thomas, R. D., Zhaunerchyk, V., Geppert, W. D., et al. (2005). Rate constants and branching ratios for the dissociative recombination of $CO_2^+$. *The Journal of Chemical Physics*, *122*(22), 226101. https://doi.org/10.1063/1.1926283

Yoshino, K., Esmond, J. R., Sun, Y., Parkinson, W. H., Ito, K., & Matsui, T. (1996). Absorption cross section measurements of carbon dioxide in the wavelength region 118.7–175.5 nm and the temperature dependence. *Journal of Quantitative Spectroscopy and Radiative Transfer*, *55*(1), 53–60. https://doi.org/10.1016/0022-4073(95)00135-2